Applied Physics A (2022) 128:954
https://doi.org/10.1007/s00339-022-06105-8

Applied Physics A
Materials Science & Processing

Phase evolution, dielectric and conductivity behaviors of $(K_{0.5}Na_{0.5})NbO_3$–$La(Zn_{0.5}Zr_{0.5})O_3$ ceramics

Yongbao Cui[1] · Tianxiang Yan[1] · Zhaohui Wang[1] · Haochen Sun[1] · Xiuyun Lei[1] · Shiguang Yan[2] · Liang Fang[1] · Laijun Liu[1,3]

Received: 28 July 2022 / Accepted: 30 September 2022 / Published online: 7 October 2022

Abstract

$(1-x)K_{0.5}Na_{0.5}NbO_3$–$xLa(Zn_{0.5}Zr_{0.5})O_3$ [$(1-x)$KNN–xLZZ, $x=0.005$, 0.010, 0.015, 0.020] ceramics were synthesized to fulfill the application requirement of high-temperature ceramic capacitors. The influence of LZZ content on the phase structure, microstructure morphology, dielectric and conductivity behaviors of this system was conducted. An orthorhombic phase for $0.005 \le x \le 0.010$ and an orthorhombic-tetragonal coexisting phase for $0.015 \le x \le 0.020$ were determined by the X-ray diffraction, Rietveld refinement, and dielectric spectra. The ceramic with $x=0.015$ exhibits an ultrahigh and stable permittivity ($\varepsilon' \sim 1892$, $\pm 15\%$ variation) and a low dielectric loss ($\tan\delta \le 0.05$) in a wide temperature region of 82–382 °C owing to the composition heterogeneity-induced shoulder-like peak and diffuse phase transition from tetragonal to cubic. The activation energies from the high-temperature dielectric relaxation and conductivity behaviors initially enhance greatly and then increase slowly, which could be related to the synergy effect of decreased oxygen vacancies and microstructure morphology evolution.

Keywords Ceramic · Permittivity · Dielectric loss · Oxygen vacancies

1 Introduction

Ceramic capacitors with coupling, filtering, bypass, and other functions are the core electronic components in many fields such as computer, mobile phone, and motor vehicle. The actual temperature of widely used $BaTiO_3$-based X8R ceramic capacitors is restrained to 150 °C due to their low Curie temperature (T_c) [1, 2]. However, some harsh operational conditions (e.g., engine control, deep oil exploration) express the development demand of high-temperature ceramic capacitors (HTCC) that operate stably above 200 °C or even 300 °C [3, 4]. Moreover, the development direction of HTCC is high reliability, small volume, and eco-friendliness. Therefore, to fulfill the practical working requirement of HTCC, lead-free dielectric ceramics with a high and stable permittivity (ε') and a low dielectric loss ($\tan\delta$) across a broad temperature range have received considerable concern [5–20].

Perovskite oxides have drawn much attention in diverse electrical devices owing to their excellent dielectric, pyroelectric, piezoelectric, ferroelectric, photoelectric, and catalytic properties [10–27]. In recent years, a great number of lead-free dielectric materials with perovskite structure for HTCC application have been extensively investigated, e.g., $BaTiO_3$-based [5, 6], $Bi_{0.5}Na_{0.5}TiO_3$-based [7–9], and $K_{0.5}Na_{0.5}NbO_3$ (KNN)-based dielectric ceramics [10, 11]. Among them, KNN-based ceramics by composition modulation are considered to be potential materials for HTCC application [10–12]. Generally, unmodified KNN ceramic presents an intense temperature dependence of permittivity which is caused by two phase transitions from tetragonal to cubic ($T_C \sim 410$ °C) and orthorhombic to tetragonal ($T_{O\text{-}T} \sim 200$ °C) [12]. An alternative approach that improves

✉ Tianxiang Yan
yangtxboy@163.com

[1] College of Mechanical and Control Engineering and College of Materials Science and Engineering, Guilin University of Technology, Guilin 541004, China

[2] Key Laboratory of Inorganic Functional Materials and Devices, Shanghai Institute of Ceramics, Chinese Academy of Sciences, 1295 Dingxi Road, Shanghai 200050, China

[3] Collaborative Innovation Center for Exploration of Nonferrous Metal Deposits and Efficient Utilization of Resources in Guangxi, Guilin University of Technology, Guilin 541004, China

its temperature stability of permittivity is to achieve a ferroelectric relaxor with diffuse phase transition by introducing dopants or forming solid solutions [13–18].

The Bi-based ABO_3-type perovskites are usually used to obtain good temperature stability of permittivity in KNN-based solid solutions [13–17]. For example, $Bi(Zn_{2/3}Nb_{1/3})O_3$-doped KNN was reported to show a stable permittivity from 79 to 342 °C [17]. However, the volatilization of bismuth during sintering at high temperature produces intrinsic oxygen vacancies, leading to the increase of high-temperature dielectric loss. Recently, Liu et al. reported that the $La(Zn_{0.5}Ti_{0.5})O_3$-modified KNN showed a stable permittivity with a low tanδ in a wide temperature region of 95–350 °C [18]. Furthermore, the relaxor feature with diffuse phase transition has been found in the KNN–$AZrO_3$ [A = Ba^{2+}, Sr^{2+}] solid solutions [19, 20], which can effectively enhance the temperature stability of permittivity and broaden the operational temperature range.

Combined with the above studies, it is anticipated that the introduction of $La(Zn_{0.5}Zr_{0.5})O_3$ into KNN can produces excellent dielectric properties for HTCC application. Therefore, $La(Zn_{0.5}Zr_{0.5})O_3$-doped KNN ceramics were prepared. To get deep insight into the dielectric properties of this system, the phase evolution was identified by X-ray diffraction (XRD), Rietveld refinement, and dielectric spectra, and the dielectric relaxation and conductivity behaviors at high temperature were characterized by the Arrhenius law and the universal dielectric response (UDR) law.

2 Experimental procedure

Lead-free $(1-x)K_{0.5}Na_{0.5}NbO_3$–$xLa(Zn_{0.5}Zr_{0.5})O_3$ [$(1-x)$KNN–xLZZ, x = 0.005, 0.010, 0.015, 0.020] ceramics were synthesized using the raw powders Na_2CO_3 (99.8%), K_2CO_3 (99%), Nb_2O_5 (99.9%), La_2O_3 (99.99%), ZnO (99.99%), and ZrO_2 (99.99%) (Shanghai Aladdin Bio-Chem Technology Co., Ltd., China) by a solid state sintering route. First, these powders were fired in an oven of 120 °C for 24 h and weighed according to the nominal $(1-x)$KNN–xLZZ ratios, then ball-milled for 12 h and calcined at 900 °C for 4 h. Second, the calcined powders were re-milled for 12 h, then fired and ground with a 5 wt% polyvinyl alcohol (PVA) binder. Finally, the resultant powders were pressed into pellets 10 mm in diameter at ~ 350 MPa, and the pellets covered with the same composition powders were sintered at 1150–1160 °C for 4 h in an alumina crucible.

The phase structure of $(1-x)$KNN–xLZZ samples at room temperature was measured using an automatic X-ray diffractometer (PANalytical, X'Pert PRO, Netherlands) with Cu K_α radiation. The structural parameters were obtained using the Rietveld refinement of GSAS program. The microstructure morphology of thermally etched samples with painted gold was observed using a scanning electron microscopy (SEM, JSM 6380, Japan). The density and porosity percentage were obtained by the Archimedes method. For the dielectric test, the sintered pellets were polished, and two surfaces were brushed with silver paste and then heated up to 650 °C for 0.5 h to generate the electrodes. The permittivity (ε') and dielectric loss (tanδ) from room temperature (RT) to 550 °C and the impedance data at 20 Hz–1 MHz in a temperature range of 480–560 °C were recorded using a high-precision LCR meter (KEYSIGHT E4980AL, USA).

3 Results and discussion

The XRD patterns of $(1-x)$KNN–xLZZ ceramics at RT in a reflection angle (2θ) range of 20–60° are displayed in Fig. 1a. The magnified XRD patterns from 44° to 47° are shown in Fig. 1b. It can be seen from Fig. 1a that all the samples have a single perovskite structure except that an impurity of $K_6Nb_{10.8}O_{30}$ indexed by X'Pert HighScore Plus software appears in the sample with x = 0.005. It indicates that LZZ has diffused into the KNN matrix to obtain the $(1-x)$KNN–xLZZ solid solution. Moreover, according to the peak shape in Fig. 1b, the small addition of LZZ dramatically changes the phase structure of KNN. The samples with x = 0.005 and 0.010 have an orthorhombic phase (*Amm*2) similar to pristine KNN, which is characterized by the intensity of (022) peak higher than that of the (200) peak near 45° [28, 29]. With further increase in LZZ, the sample with x = 0.015 evolved into an orthorhombic and tetragonal coexisting phase based on the intensity of (022)/(002) peak close to that of the (200) peak, which is in accordance with the $Bi(Zn_{2/3}Nb_{1/3})O_3$-modified KNN system [17]. Although the sample with x = 0.020 shows a typical tetragonal phase (*P*4*mm*) characteristic of the higher intensity of the (200) peak than that of the (002) peak in the vicinity of 45° [29],

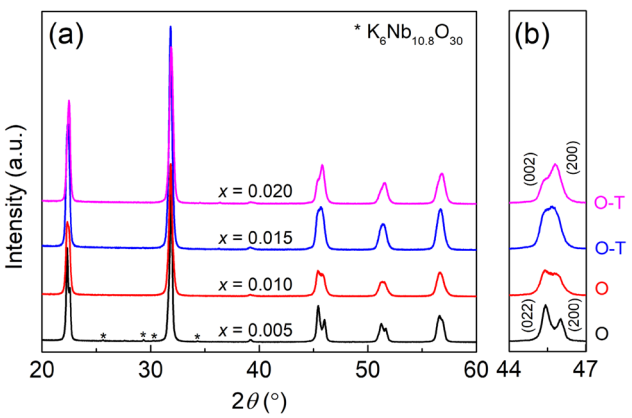

Fig. 1 XRD patterns of $(1-x)$KNN–xLZZ ceramics: 2θ **a** from 20° to 60° and **b** from 44° to 47°

the following Rietveld refinement and dielectric spectra confirm that it still maintains the orthorhombic and tetragonal coexisting phase.

To better understand the phase structure evolution of $(1-x)$KNN–xLZZ ceramics, the Rietveld refinement of the measured XRD data was carried out using the GSAS software. The space groups were specified according to the XRD results and the incipient crystal parameters were adopted from Ref. [30]. During the structural refinement, the relevant parameters (e.g., scale factor, background, cell parameters) were continuously adjusted to decrease the difference between the measured XRD data and fitted values. The refinement results (e.g., observation, calculation, and difference values) are shown in Fig. 2. The small difference values suggest that the measured XRD data are well matched to the refined model. The crystal parameters, weighted profile residual factor (R_{wp}), and profile residual factor (R_p) are listed in Table 1. The R_{wp} and R_p factors of 4–8% prove the rationality of the phase structure.

As shown in the inset of Fig. 2, the *Amm*2 and *P*4*mm* unit cells contain two octahedral units and one octahedral unit, respectively. From the cell volume of Table 2, the average volume of the octahedral unit can be calculated: 63.2080 Å^3 for $x=0.005$, 63.1327 Å^3 for $x=0.010$, 63.0343 Å^3 for $x=0.015$, and 62.9976 Å^3 for $x=0.020$. The average volume of the octahedral unit has a slight decrease with increasing LZZ, which is associated with ionic substitution. For the $(1-x)$KNN–xLZZ solid solution, according to the radius match rule of ABO_3-type perovskite structure, the K^+ [1.64 Å, coordination number (CN) = 12], Na^+ (1.39 Å, CN = 12) and La^{3+} (1.34 Å, CN = 12) with larger size occupy the A site, whereas the Nb^{5+} (0.64 Å, CN = 12), Zn^{2+} (0.74 Å, CN = 12) and Zr^{4+} (0.72 Å, CN = 12) with smaller size occupy the B site [31]. Consequently, the incorporation of LZZ into KNN slightly shrinks the average volume of the octahedral unit.

The SEM morphology of $(1-x)$KNN–xLZZ ceramics is shown in Fig. 3a–d. The samples with $0.005 \le x \le 0.015$ present dense microstructure with few pores in Fig. 3a–c. With further increase in LZZ, a great number of pores are generated in the sample with $x=0.020$ as in Fig. 3d. Figure 4a–d presents the distribution of grain sizes of different samples measured by the ImageJ software. The calculated average grain sizes are 7.84 μm, 5.04 μm, 11.22 μm, and

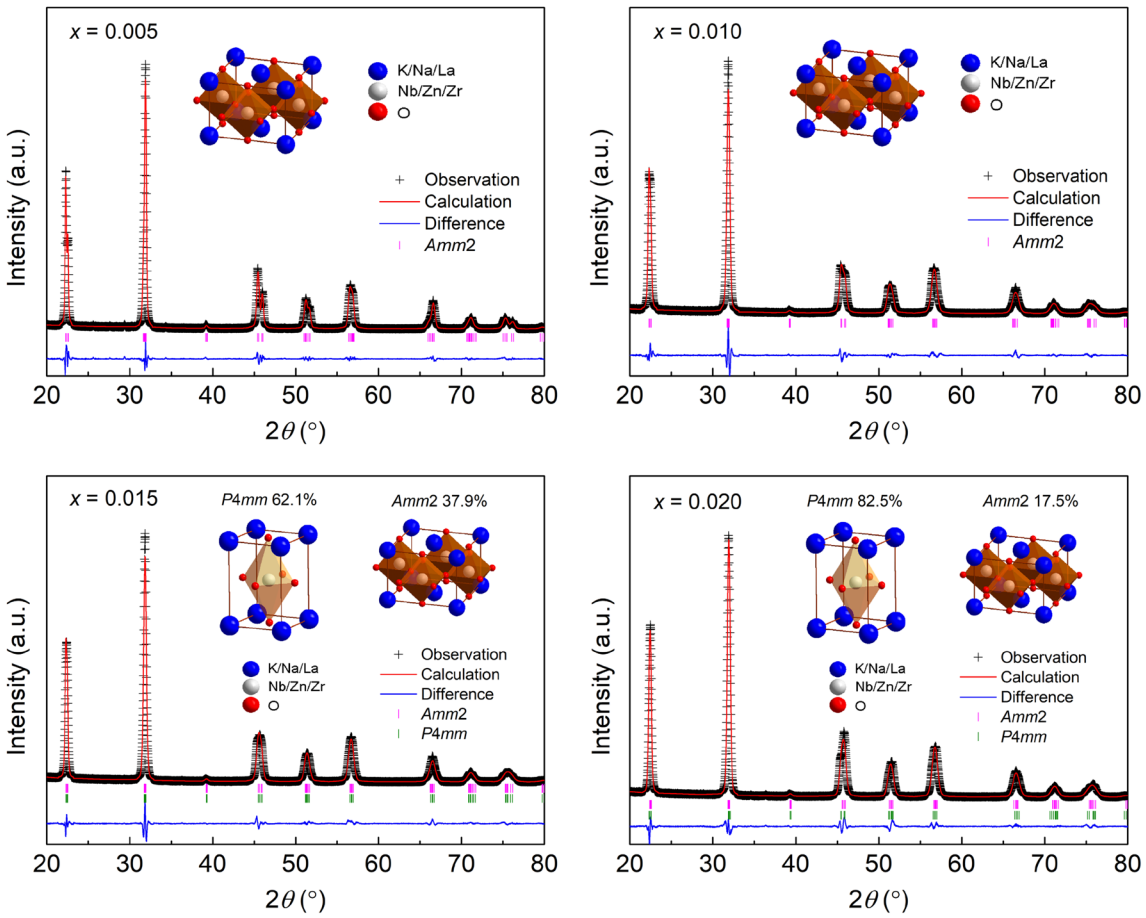

Fig. 2 Rietveld refinement results for $(1-x)$KNN–xLZZ ($x=0.005$, 0.010, 0.015, and 0.020) ceramics at RT

Table 1 Crystal parameters, R_{wp}, and R_p of Rietveld refinement for $(1-x)$KNN–xLZZ ($x=0.005$, 0.010, 0.015, and 0.020) ceramics at RT

Composition	$x=0.005$	$x=0.010$	$x=0.015$		$x=0.020$	
Space group	*Amm*2	*Amm*2	*Amm*2	*P*4*mm*	*Amm*2	*P*4*mm*
Symmetry	Orthorhombic	Orthorhombic	Orthorhombic	Tetragonal	Orthorhombic	Tetragonal
Phase fraction	100%	100%	37.9%	62.1%	17.5%	82.5%
a (Å)	3.95389(5)	3.95675(10)	3.95862(10)	3.98985(7)	3.96362(29)	3.96713(9)
b (Å)	5.66687(16)	5.6528(8)	5.6456(12)	3.98985	5.6450(16)	3.96713
c (Å)	5.64200(17)	5.6452(7)	5.6395(12)	3.96031(12)	5.6293(16)	4.00314(14)
$\alpha/\beta/\gamma$	90.0	90.0	90.0	90.0	90.168(7)	90.0
V (Å^3)	126.4160(30)	126.265(4)	126.036(4)	63.0440(20)	125.953(10)	63.0020(20)
x (K/Na/Bi)	0.0	0.0	0.0	0.0	0.0	0.0
y (K/Na/Bi)	0.0	0.0	0.0	0.0	0.0	0.0
z (K/Na/Bi)	0.00746	0.00848	0.01174	0.01833	0.0263	0.0231
x (Nb/Zn)	0.5	0.5	0.5	0.5	0.5	0.5
y (Nb/Zn)	0.0	0.0	0.0	0.5	0.0	0.5
z (Nb/Zn)	0.49129	0.493	0.5151	0.47925	0.51357	0.48337
x (O1)	0.0	0.0	0.0	0.5	0.0	0.5
y (O1)	0.0	0.0	0.0	0.5	0.0	0.5
z (O1)	0.48064	0.4572	0.45554	0.01668	0.43082	0.00811
x (O2)	0.5	0.5	0.5	0.5	0.5	0.5
y (O2)	0.26544	0.25742	0.26616	0.0	0.28093	0.0
z (O2)	0.26566	0.27176	0.28064	0.50655	0.28427	0.50329
R_{wp} (%)	7.09	7.42	6.69		6.62	
R_p (%)	5.23	5.56	5.06		4.86	

Table 2 Dielectric properties of the 0.985KNN–0.015LZZ ceramic and some reported KNN-based HTCC ceramics

Compound	ε'_{mid} at T (°C)	T range for Tanδ (°C)	T range for $\Delta\varepsilon'/\varepsilon'_{mid}$ (°C)	Refs.
0.985KNN–0.015LZZ	~ 1892 (270)	63–443 ≤ 5%	83–382 ≤ 15%	This work
$0.9K_{0.5}Na_{0.5}NbO_3$–$0.1(Ba_{0.5}Sr_{0.5})TiO_3$	~ 1500 (150)	25–350 ≤ 4%	25–350 ≤ 15%	[10]
$0.92K_{0.5}Na_{0.5}NbO_3$–$0.08(Bi_{0.5}Li_{0.5})ZrO_3$	~ 1317 (200)	120–400 ≤ 6%	55–445 ≤ 15%	[16]
$0.98K_{0.5}Na_{0.5}NbO_3$–$0.02Bi(Zn_{2/3}Nb_{1/3})O_3$	~ 1310 (300)	75–342 ≤ 5%	79–433 ≤ 15%	[17]
$0.98K_{0.5}Na_{0.5}NbO_3$–$0.02La(Zni_{0.5}Ti_{0.5})O_3$	~ 1560 (150)	58–480 ≤ 3%	96–350 ≤ 15%	[18]
$0.9K_{0.5}Na_{0.5}NbO_3$–$0.1Bi(Zn_{0.75}W_{0.25})O_3$	~ 1300 (150)	50–470 ≤ 5%[a]	150–350 ≤ 15%	[36]

[a]Estimated values from diagrams in the cited references

12.94 μm for the samples with $x=0.005$, 0.010, 0.015, and 0.020, respectively. The average grain size initially declines for $0.005 \le x \le 0.010$ and then increases with further increase of LZZ content. The decrease of average grain size could be because a low concentration of La^{3+} aggregates at the grain boundary to restrict the grain growth and a similar phenomenon was also observed in the La-modified KNN ceramics [32]. The increase of average grain size could be beacuse ZnO promotes grain growth at the sintering aid due to its low melting point and liquid-phase effect similar to the ZnO- and MnO_2-added KNN system [33]. In addition, the densities of the samples with $x=0.005$, 0.010, 0.015, and 0.020 are 4.36 g/cm^3, 4.38 g/cm^3, 4.33 g/cm^3, and 4.23 g/cm^3, respectively. The porosity percentages of the samples with $x=0.005$, 0.010, 0.015, and 0.020 are 4.73%, 3.02%, 4.93%, and 8.64%, respectively. It can be found that the density and porosity percentage of $0.005 \le x \le 0.015$ are both much higher than those of $x=0.020$, which is in agreement with the result of microstructure morphology.

The temperature dependent permittivity (ε') of $(1-x)$KNN–xLZZ ceramics at 100 kHz is shown in Fig. 5. Similar to pristine KNN, the samples with $x=0.005$ and 0.010 present the permittivity peaks of T_m and $T_{O\text{-}T}$ higher than RT, indicating an orthorhombic phase at RT. With the increase of LZZ, T_m rapidly shifts to a lower temperature. It is notable that the samples with $x=0.010$, 0.015 and 0.020 exhibit a shoulder-like peak (T_s) around 380 °C. Such a shoulder-like peak could be attributed to the composition heterogeneity (core–shell structure) and a similar phenomenon has been also reported in the KNN–$AZrO_3$ ($A=Sr^{2+}$, $(Bi_{0.5}K_{0.5})^{2+}$)

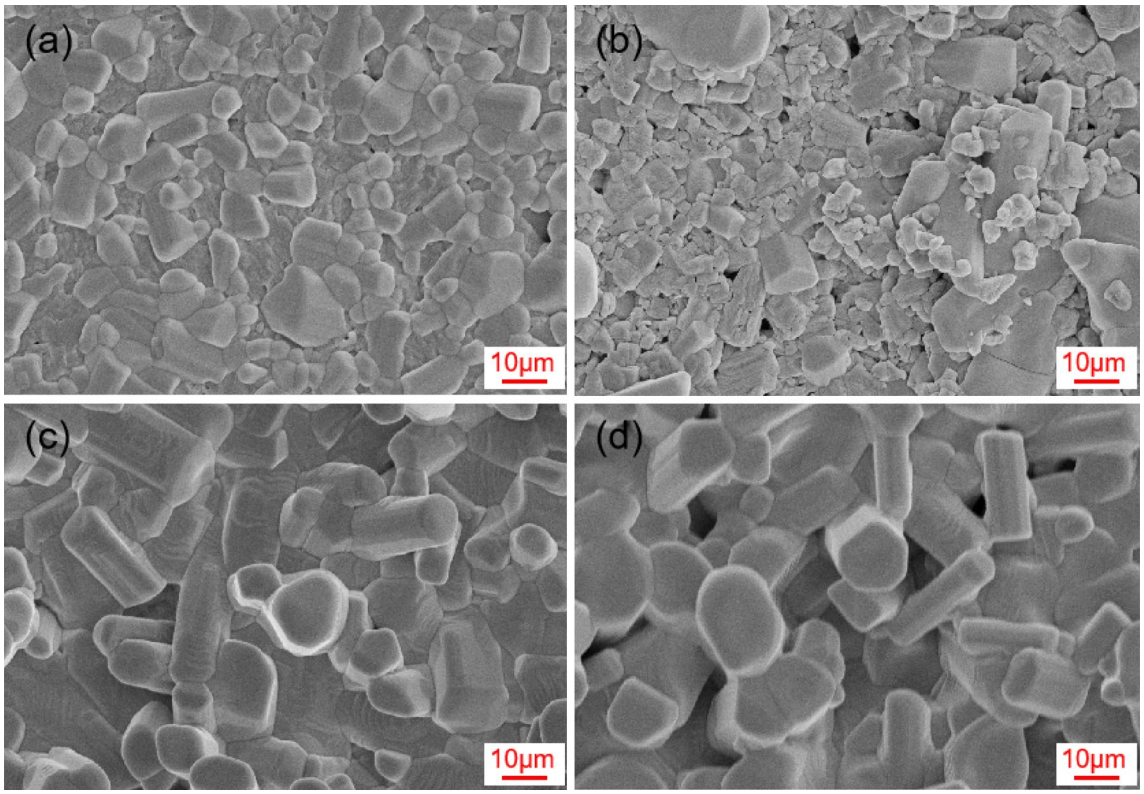

Fig. 3 SEM morphology of $(1-x)$KNN–xLZZ ceramics: **a** $x=0.005$, **b** $x=0.010$, **c** $x=0.015$, and **d** $x=0.020$

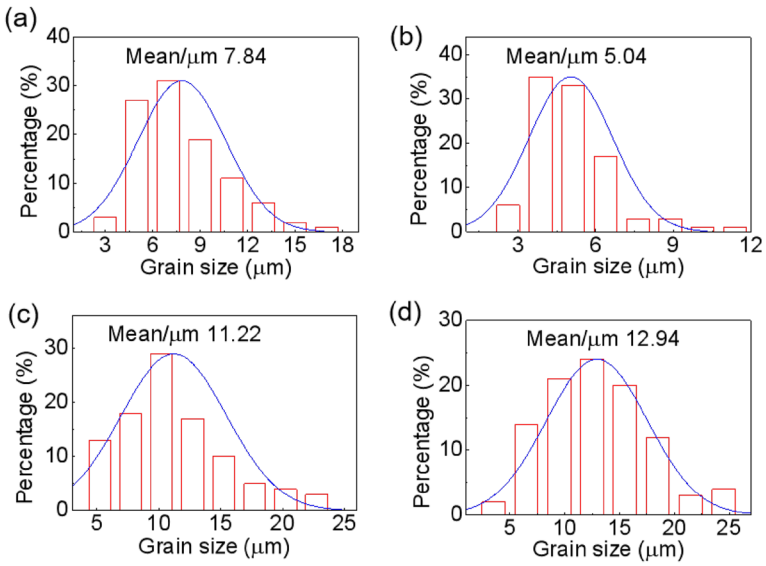

Fig. 4 Distribution of grain sizes of $(1-x)$KNN–xLZZ ceramics: **a** $x=0.005$, **b** $x=0.010$, **c** $x=0.015$, and **d** $x=0.020$

solid solutions [20, 34]. As a result, the samples with $x=0.015$ and 0.020 possess an orthorhombic and tetragonal coexisting phase, which is consistent with the analysis of XRD and Rietveld refinement. However, the composition heterogeneity distribution cannot be found by energy-dispersive spectroscopy (EDS) owing to the slight element difference. In addition, the samples with $0.015 \le x \le 0.020$ exhibit a low-temperature diffuse phase transition from tetragonal to cubic, which has been largely reported in the ferroelectric relaxors [34–37]. Such a diffuse phase transition in this study is assigned to the thermal evolution of polar nano-regions (PNRs) size/volume produced by the

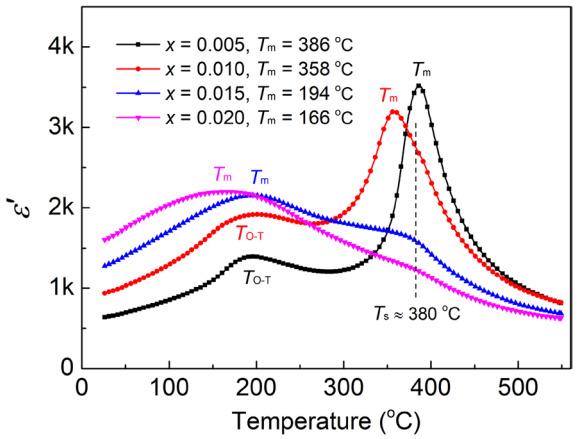

Fig. 5 Temperature dependent permittivity (ε') for $(1-x)$KNN–xLZZ ceramics with different LZZ contents at 100 kHz

heterovalent ion substitutions (e.g., La^{3+} for $(K_{0.5}Na_{0.5})^{+}$ at the A site, $(Zn_{0.5}Zr_{0.5})^{3+}$ for Nb^{5+} at B site). Consequently, the temperature stability of permittivity for the samples with $x=0.015$ is significantly improved owing to the composition heterogeneity-induced shoulder-like peak and the diffuse phase transition from tetragonal to cubic.

The temperature stability of permittivity is a key indicator for practical application of HTCC materials. In Fig. 6a, the temperature variation of permittivity ($\Delta\varepsilon'/\varepsilon'_{270\ °C}$, $\Delta\varepsilon'=\varepsilon'-\varepsilon'_{270\ °C}$) for $(1-x)$KNN–xLZZ ceramics at 100 kHz shows that the addition of LZZ has a great effect on the temperature stability of permittivity. Especially, the sample with $x=0.015$ exhibits a wide operational temperature range of 82–382 °C based on the ±15% tolerance of Electronic Industries Alliance (EIA) X8R capacitor standards [17, 18], as shown by the gray box in Fig. 6a. The temperature-dependent dielectric loss (tanδ) for $(1-x)$KNN–xLZZ ceramics at 100 kHz is shown in Fig. 6b. The tanδ of the sample with $x=0.015$ is maintained low (≤0.05), from 63 to 443 °C. The dielectric properties of the 0.985KNN–0.015LZZ ceramic and some reported KNN-based HTCC ceramics are listed in Table 2 [10, 16–18, 36]. By a comparison of the dielectric properties, the 0.985KNN–0.015LZZ ceramic with an ultra-high and stable ε' (~1892, ±15% variation) and a low tanδ (≤5%) from 82 to 382 °C is a potential candidate for HTCC application. It is notable that tanδ of the samples increases dramatically above 450 °C, which is related to a thermally induced conductivity behavior [8, 38].

To provide a better understanding of the conductivity behavior of $(1-x)$KNN–xLZZ ceramics at high temperature, the normalized imaginary parts of impedance (Z''/Z''_{max}) for this system as a function of frequency at measured temperatures are shown in Fig. 7a–d. For each temperature of different samples, the measured frequency region shows an asymmetric peak. With the increase in temperature, the peak/relaxation frequency (f_{max}) gradually shifts toward a higher frequency, which suggests a thermally induced relaxation behavior [39, 40]. This relaxation behavior is because increase in temperature promotes the hopping/migration of charge carriers (e.g., holes, electrons, ions). Generally, the connection between f_{max} and the relevant temperature can be expressed using the following Arrhenius equation:

$$f_{max} = f_0 \exp\left(\frac{-E_{rel}}{k_B T}\right), \tag{1}$$

where f_0 is the pre-constant, E_{rel} denotes the activation energy from relaxation behavior, and k_B and T denote the Boltzmann constant (8.617×10^{-5} eV/K) and kelvin temperature (K), respectively. The Arrhenius plots of relaxation frequency (f_{max}) were fitted based on Eq. (1), as shown by the straight lines in Fig. 8. The E_{rel} values can be solved according to the slope of fitted straight lines: $E_{rel}=1.264$ eV for $x=0.005$, $E_{rel}=1.352$ eV for $x=0.010$, $E_{rel}=1.440$ eV

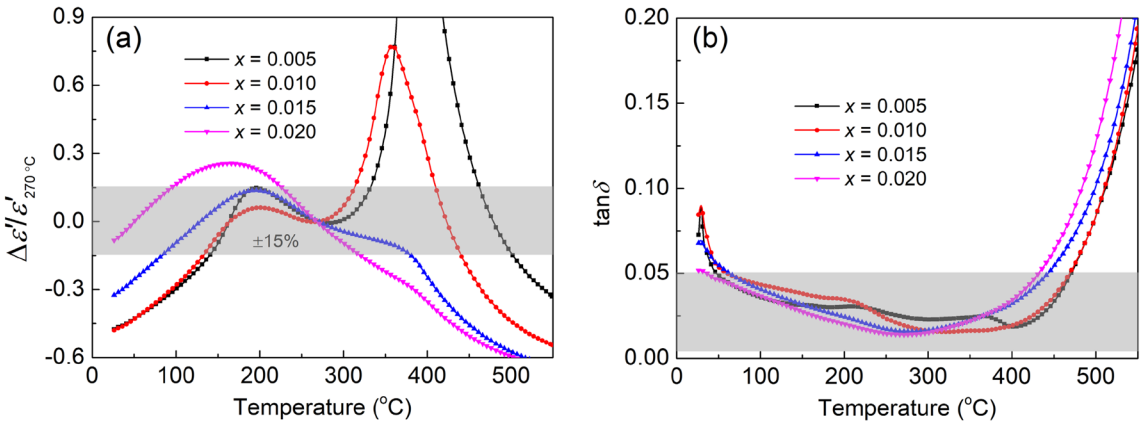

Fig. 6 Temperature stability range of **a** permittivity (ε') and **b** dielectric loss (tanδ) for $(1-x)$KNN–xLZZ ($x=0.005$, 0.010, 0.015, and 0.020) ceramics at 100 kHz

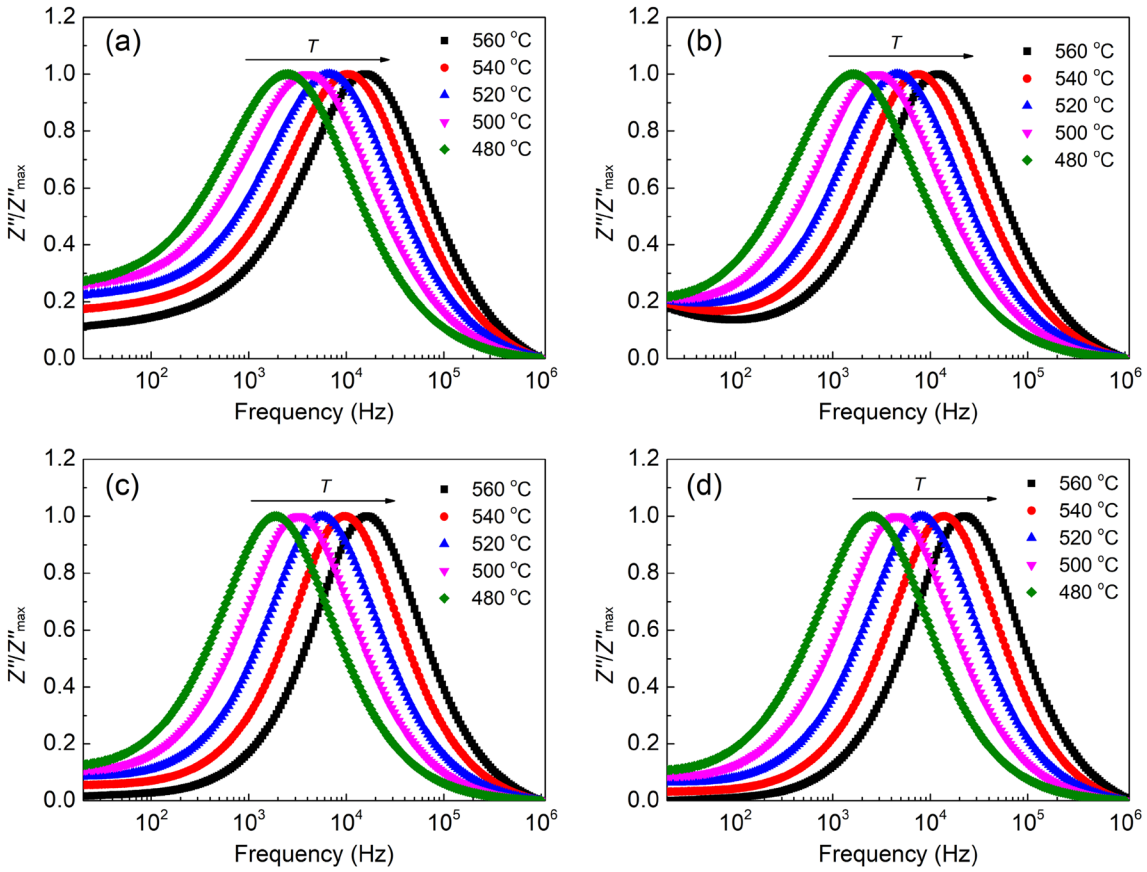

Fig. 7 Normalized imaginary parts of impedance (Z''/Z''_{max}) for $(1-x)$KNN–xLZZ ceramics as a function of frequency at measured temperatures: **a** $x=0.005$, **b** $x=0.010$, **c** $x=0.015$, and **d** $x=0.020$

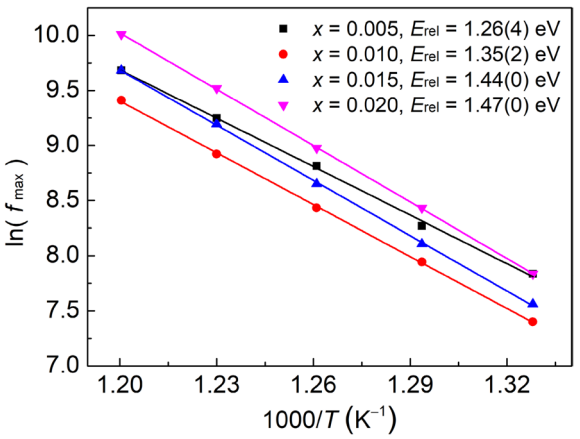

Fig. 8 Arrhenius plots of relaxation frequency for $(1-x)$KNN–xLZZ ceramics with different LZZ contents. The straight lines are linear fitting

for $x=0.015$, and $E_{rel}=1.470$ eV for $x=0.020$. The E_{rel} monotonously increases with the increase in LZZ.

The frequency-dependent AC conductivity (σ_{AC}) of $(1-x)$KNN–xLZZ ceramics at measured temperatures is shown in Fig. 9a–d. With increasing frequency, σ_{AC} initially presents a constant platform close to the DC conductivity (σ_{DC}) and then significantly increases, due to the contribution of localized charge carriers' hopping/migration to conductivity. This conductivity behavior originates from the many-body interplay between the dipoles and charge carriers, which can be expressed using the following universal dielectric response (UDR) equation [39, 40]:

$$\sigma_{AC} = \sigma_{DC} + \sigma_0 f^s, \tag{2}$$

where σ_0, f and s are the pre-constant, probing frequency, and exponent factor $(0<s\leq 1)$, respectively. As shown by the red lines in Fig. 9, the nonlinear fitting between σ_{AC} and probing frequency was carried out and the σ_{DC} was solved based on Eq. (2). The connection between the obtained σ_{DC} and relevant temperature can be expressed using the following Arrhenius equation:

$$\sigma_{DC} = \sigma_1 \exp\left(-\frac{E_{con}}{k_B T}\right), \tag{3}$$

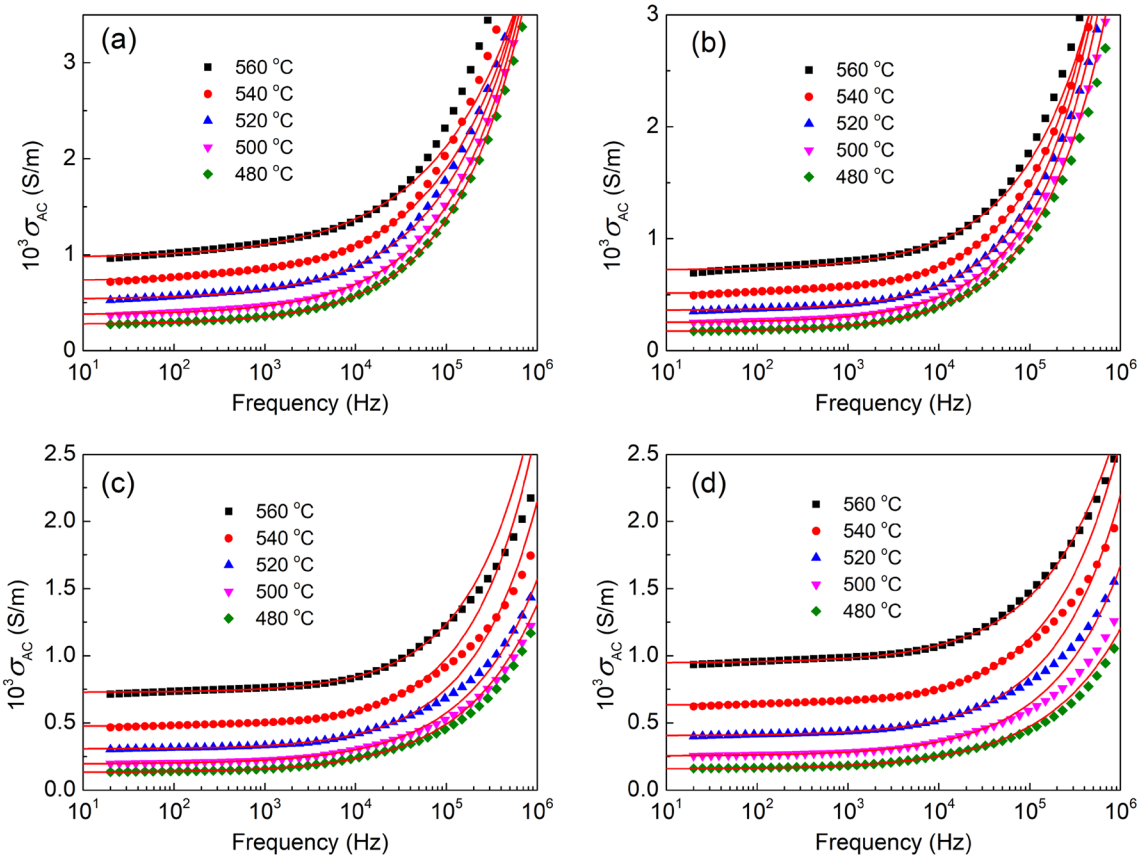

Fig. 9 Frequency-dependent AC conductivity (σ_{AC}) of $(1-x)$KNN–xLZZ ceramics at the measured temperatures: **a** $x=0.005$, **b** $x=0.010$, **c** $x=0.015$, and **d** $x=0.020$. The red lines are nonlinear fitting based on Eq. (2)

where σ_1 is the pre-constant and E_{con} denotes the activation energy from DC conductivity. The Arrhenius plots of DC conductivity (σ_{DC}) were fitted based on Eq. (3), as shown by the straight lines in Fig. 10. The E_{con} values can be solved according to the slope of fitted straight lines: $E_{con}=0.856$ eV for $x=0.005$, $E_{con}=0.968$ eV for $x=0.010$, $E_{con}=1.171$ eV for $x=0.015$, and $E_{con}=1.222$ eV for $x=0.020$. The variation trend of E_{con} is consistent with that of E_{rel}. Furthermore, the E_{rel} values are higher than those of E_{con} for all the samples. Generally, E_{rel} includes the free energy of localized charge carriers' hopping/migration between the neighboring lattice sites, whereas E_{con} contains both the long-distance hopping/migration and creation of free energies of charge carriers [41, 42]. Thus, the difference between E_{rel} and E_{con} is mainly connected with the creation of charge carriers, suggesting that charge carriers are released from the traps.

As one of the most common charged carriers in perovskite oxides, oxygen vacancies play a crucial part in high-temperature conductivity behavior. Previous studies have reported that the activation energy is in the range of 0.3–0.5 eV and 0.6–1.2 eV for the single-ionized and doubly ionized oxygen vacancies, respectively [43]. According to the E_{con} and E_{rel} values of all the samples, the doubly ionized

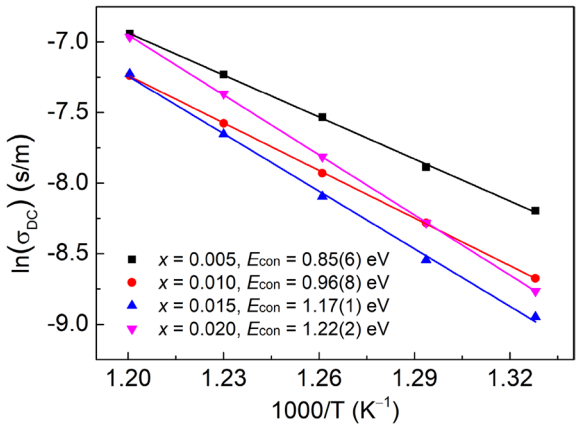

Fig. 10 Arrhenius plots of DC conductivity (σ_{DC}) for $(1-x)$KNN–xLZZ ceramics with different LZZ contents. The straight lines are linear fitting

oxygen vacancies are regarded as the dominant charged carriers of $(1-x)$KNN–xLZZ ceramics at high temperature. In the sintering process of KNN ceramic, oxygen vacancies are easily produced due to the volatility of K/Na from the lattice sites. Nevertheless, the substitution of LZZ into KNN does

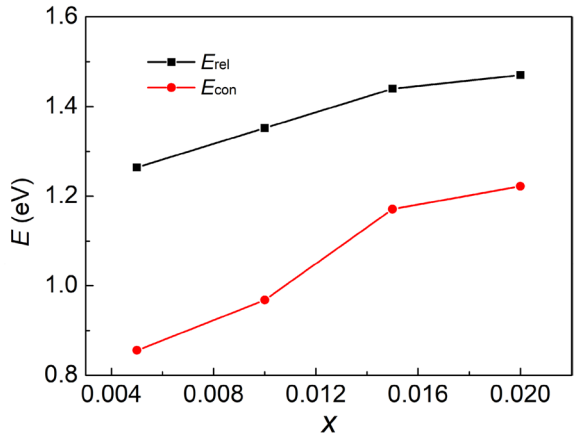

Fig. 11 Activation energies (E_{rel} and E_{con}) as a function of LZZ content (x)

not generate the oxygen vacancies compensation, because all charged carriers produced from the La^{3+} are balanced by Zn^{2+} and Zr^{4+} [44]. The relevant Kroger–Vink equations can be described as:

$$A_A \rightarrow A + V'_A + 0.5V^{\cdot\cdot}_O, \quad (4)$$

$$La_{La} + 0.5Zn_{Zn} + 0.5Zr_{Zr} \rightarrow La^{\cdot\cdot}_A + 0.5Zn'''_{Nb} + 0.5Zr'_{Nb}, \quad (5)$$

where V'_A, $V^{\cdot\cdot}_O$, $La^{\cdot\cdot}_A$, Zn'''_{Nb}, and Zr'_{Nb} are the K/Na vacancy, doubly ionized oxygen vacancies, La^{3+} at the K^+/Na^+ site, Zn^{2+} at the Nb^{5+} site, and Zr^{4+} at the Nb^{5+} site, respectively. According to Eqs. (4) and (5), the introduction of LZZ decreases the concentration of oxygen vacancies, leading to the increase of activation energy in agreement with the variation trend of E_{con} and E_{rel}. It is notable that with the addition of LZZ, both E_{rel} and E_{con} initially enhance greatly for $0.005 \le x \le 0.015$ and then increase slowly for $0.015 \le x \le 0.020$, as shown in Fig. 11. Generally, the variation trend of activation energy is associated with the oxygen vacancy concentration, microstructure morphology, and lattice deformation [15–18]. Since the LZZ content has little effect on the octahedral unit volume of $(1-x)$KNN–xLZZ solid solution from the Rietveld refinement results, such a variation trend of activation energy is considered to be associated with the oxygen vacancy concentration and microstructure morphology. With the increase of LZZ, the samples with $0.005 \le x \le 0.015$ are all dense and the decreased oxygen vacancy concentration plays a major part in the great enhancement of activation energy. With further increase in LZZ content up to $x = 0.020$, the generation of a great number of pores gives rise to the large surface on the grains [42], and the slight increase of activation energy could be attributed to the synergy effect of decreased oxygen vacancy concentration and increased pore numbers.

4 Conclusions

$(1-x)$KNN–xLZZ ceramics were synthesized by the solid state sintering method. The combined analysis of XRD, Rietveld refinement, and dielectric spectra indicates that the introduction of LZZ into KNN induces a change of crystal structure from an orthorhombic phase for $0.005 \le x \le 0.010$ to an orthorhombic–tetragonal coexisting phase for $0.015 \le x \le 0.020$ and a decrease of octahedral unit volume. Owing to the composition heterogeneity-induced shoulder-like dielectric peak and diffuse phase transition from tetragonal to cubic, the 0.985KNN–0.015LZZ ceramic exhibits a ultrahigh and stable ε' (~ 1892, ± 15% variation) and a low $\tan\delta$ (≤ 0.05) in a wide temperature region of 82–382 °C, which is a potential candidate for HTCC application. The activation energies from the high-temperature dielectric relaxation and conductivity behaviors initially enhance greatly, attributed to the decline of oxygen vacancy concentration, and then increase slowly due to the synergy effect of decreased oxygen vacancy concentration and increased pore numbers.

Acknowledgements This work was financially supported by the Natural Science Foundation of China (Grant No. 12264012), the Natural Science Foundation of Guangxi (Nos. 2019GXNSFBA245069, GA245006, AA21238001, ZY22096019, BA297029, and AD18281042); Opening Project of Key Laboratory of Inorganic Functional Materials and Devices, Chinese Academy of Sciences (No. KLIFMD202207); Guilin University of Technology (No. GUTQDJJ20176612037); the High Level Innovation Team and Outstanding Scholar Program of Guangxi Institutes.

References

1. K. Kobayashi, M. Ryu, Y. Doshida et al., J. Am. Ceram. Soc. **96**, 531 (2013)
2. J. Watson, G. Castro, J. Mater. Sci. Mater. Electron. **26**, 9226 (2015)
3. N. Raengthon, H. Brown-Shaklee, G. Brennecka et al., J. Mater. Sci. **48**, 2245 (2013)
4. P. Ren, J. He, F. Yan et al., J. Alloy. Compd. **807**, 151676 (2019)
5. Z. Chen, G. Li, X. Sun et al., Ceram. Int. **41**, 11057 (2015)
6. R. Muhammad, Y. Iqbal, I. Reaney, J. Am. Ceram. Soc. **99**, 2089 (2016)
7. M. Acosta, J. Zang, W. Jo et al., J. Eur. Ceram. Soc. **32**, 4327 (2012)
8. Q. Xu, Z. Song, W. Tang et al., J. Am. Ceram. Soc. **98**, 3119 (2015)
9. D. Li, Y. Lin, M. Zhang et al., Chem. Eng. J. **392**, 123729 (2020)
10. H. Du, W. Zhou, F. Luo, J. Appl. Phys. **105**, 124104 (2009)
11. H. Cheng, W. Zhou, H. Du et al., J. Alloy. Compd. **579**, 192 (2013)
12. H. Zhang, X. Li, X. Chen et al., J. Electron. Mater. **48**, 4017 (2019)
13. H. Du, W. Zhou, F. Luo et al., J. Appl. Phys. **104**, 044104 (2008)
14. H. Cheng, H. Du, W. Zhou et al., J. Am. Ceram. Soc. **96**, 833 (2013)
15. Z. Liu, H. Fan, M. Li, J. Mater. Chem. C **3**, 5851 (2015)

16. T. Yan, F. Han, S. Ren et al., Appl. Phys. A Mater. **124**, 338 (2018)
17. T. Yan, K. Chen, C. Li et al., J. Adv. Ceram. **10**, 809 (2021)
18. Z. Liu, A. Zhang, X. Geng et al., Ceram. Int. **45**, 16842 (2019)
19. R. Wang, H. Bando, T. Katsumata et al., Phys. Status Solidi RRL **3**, 142 (2009)
20. Z. Liu, F. Fan, S. Lei et al., J. Eur. Ceram. Soc. **37**, 115 (2017)
21. Y. Slimani, A. Selmi, E. Hannachi et al., J. Mater. Sci: Mater. Electron. **30**, 13509 (2019)
22. Y. Slimani, A. Selmi, E. Hannachi et al., J. Mater. Sci. Mater. Electron. **30**, 9520 (2019)
23. Y. Slimani, A. Selmi, E. Hannachi et al., J. Phy. Chem. Solids **156**, 110183 (2021)
24. E. Hannachi, M. Sayyed, K. Mahmoud et al., Appl. Phys. A **127**, 970 (2021)
25. E. Hannachi, M. Sayyed, B. Albarzan et al., Ceram. Int. **47**, 28528 (2021)
26. E. Hannachi, K. Mahmoud, M. Sayyed et al., Mat. Sci. Semicon. Proc. **145**, 106629 (2022)
27. V. Jha, S. Alam et al., J. Supercond. Nov. Magn. **33**, 455 (2020)
28. R. Zuo, X. Fang, C. Ye, Appl. Phys. Lett. **90**, 092904 (2007)
29. C. Long, T. Li, H. Fan et al., J. Alloy. Compd. **658**, 839 (2016)
30. A. Hewat, J. Phys. C: Solid State Phys. **6**, 2559 (1973)
31. R. Shannon, Acta Crystallogr. **32**, 751 (1976)
32. D. Gao, K. Kwok, D. Lin et al., J. Phys. D Appl. Phys. **42**, 035411 (2009)
33. I. Kang, I. Seo, Y. Cha et al., J. Eur. Ceram. Soc. **32**, 2381 (2012)
34. T. Yan, S. Ren, X. Ma et al., J. Electron. Mater. **47**, 7106 (2018)
35. H. Du, W. Zhou, F. Luo, J. Am. Ceram. Soc. **91**, 2903 (2008)
36. X. Chen, J. Chen, D. Ma et al., Mater. Lett. **145**, 247 (2015)
37. L. Liu, M. Knapp, H. Ehrenberg et al., J. Eur. Ceram. Soc. **37**, 1387 (2017)
38. S. Zhou, T. Yan, K. Chen et al., J. Electroceram. **46**, 72 (2021)
39. M. Boukriba, F. Sediri, N. Gharbi, Mater. Res. Bull. **48**, 574 (2013)
40. X. Chen, X. Yan, X. Li et al., J. Alloy. Compd. **762**, 697 (2018)
41. Z. Abdelkafi, N. Abdelmoula, H. Khemakhem et al., J. Appl. Phys. **100**, 114111 (2006)
42. T. Li, H. Fan, C. Long et al., J. Alloys. Compd. **609**, 60 (2014)
43. L. Liu, H. Fan, L. Fang et al., Mater. Chem. Phys. **117**, 138 (2009)
44. S. Dwivedi, T. Pareek, M. Badole et al., J. Appl. Phys. **127**, 094104 (2020)